Chemical Engineering Journal 324 (2017) 26–34

Contents lists available at ScienceDirect

Chemical Engineering Journal

journal homepage: www.elsevier.com/locate/cej

Marine algae inspired pre-treated SnO_2 nanorods bundle as negative electrode for Li-ion capacitor and battery: An approach beyond intercalation

Palanichamy Sennu [a], Vanchiappan Aravindan [b], Yun-Sung Lee [a,*]

[a] Faculty of Applied Chemical Engineering, Chonnam National University, Gwang-ju 500-757, Republic of Korea
[b] Energy Research Institute @ NTU (ERI@N), Nanyang Technological University, Research Techno Plaza, 50 Nanyang Drive, Singapore 637553, Singapore

HIGHLIGHTS

- High energy Li-ion capacitor (187 Wh kg^{-1}) and battery (400 Wh kg^{-1}) is fabricated.
- Pre-treated SnO_2 is used as alloy type anode under the optimized loadings.
- Activated carbon and $Li_{0.995}V_{0.005}Ni_{0.5}Mn_{1.5}O_4$ is used as cathode for Li-ion capacitor and battery.
- Mass balance has been adjusted based on the performance with metallic Li.

GRAPHICAL ABSTRACT

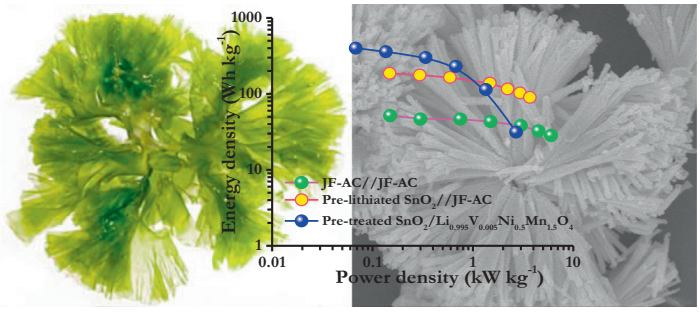

ARTICLE INFO

Article history:
Received 2 March 2017
Received in revised form 18 April 2017
Accepted 2 May 2017
Available online 4 May 2017

Keywords:
Lithium-ion battery
Lithium-ion capacitor
Supercapacitor
Alloying

ABSTRACT

Group IV elements in the form of metal or metal oxides have been intensively investigated as high performance negative electrodes for charge storage devices owing to its high theoretical capacity and relatively lower cost. In addition, such elements especially Sn based derivatives are found to be better alternatives for traditional topotactic insertion anodes like graphite and $Li_4Ti_5O_{12}$. In the present work, we report the scalable synthesis of marine inspired SnO_2 nanorods bundles by precipitation technique. The preliminary electrochemical performance of SnO_2 (half-cell studies with Li) is examined as anode at different electrolyte solutions and various loading of conductive additives. The fabrication of Li-ion capacitor (LIC) has been made using pre-lithiated SnO_2 as anode with bio-waste (Jackfruit skin) derived activated carbon as cathode under the optimized mass loadings. The LIC can deliver the maximum energy density of ~187 Wh kg^{-1} with an ~82% of initial energy retention after 10,000 charge-discharge cycles. Furthermore, the pre-treated SnO_2 also investigated as negative electrode with homemade high voltage spinel ($Li_{0.995}V_{0.005}Ni_{0.5}Mn_{1.5}O_4$) towards the construction of high-energy Li-ion battery (LIB). Similar to the LIC, the mass loading of LIB has been adjusted based on the half-cell performance with Li. The LIB can work in the potential of ~4.27 V with energy density of ~400 Wh kg^{-1} (based on total mass loading of both electrodes).

1. Introduction

Increasing solicitude about global warming and depletion of fossil fuels, the energy consumption from renewable clean sources is one of the efficient alternate approaches rather than utilising

* Corresponding author.
E-mail addresses: aravind_van@yahoo.com (V. Aravindan), leeys@chonnam.ac.kr (Y.-S. Lee).

http://dx.doi.org/10.1016/j.cej.2017.05.003
1385-8947/

conventional ones for sustainable earth. Reliable and sustainable energy storage systems are desperately required to fulfil the necessary energy demands. Currently in the electrical market, the available and extensively studied Li-ion batteries (LIB) are used and remain popular by considering its advantages like shape versatility, flexibility, high energy and long cycle life [1–4]. However, concerns over the inherent limitations, poor power capability, cost and recycling pollutions are certainly hindered their potential application to large-scale electrical-energy storage, but R&D is still underway to overcome those limitations [1]. Among the diverse systems exploited, Li-ion capacitor (LIC) is considered as a strong contender for hybrid electric vehicles (HEV), electric vehicle (EV) and grid storage [5–11]. In addition, Ioxus and JSR micro Inc., were already introduced the LIC devices in commercial market which reveals the combined advantage of both ultra-capacitor and LIB chemistry. Most of the current research activities are devoted for the development of judicious design and synthesis of electro-active materials (electrodes and electrolytes) which are vital prerequisites for the progress of high energy system with high power capability. However, in such LIC, the energy density is highly limited (<100 Wh kg^{-1}), but, beyond 150 Wh kg^{-1} is required to drive aforesaid applications [7,8,12]. This is mainly because of the limited Li-ion diffusion kinetics in insertion type electrodes like graphite, hard carbon, $Li_4Ti_5O_{12}$ etc. Thus, improving the energy density of LIC by altering supercapacitor component *i.e.* high surface area carbonaceous material (activated carbon, AC) is highly limited owing to its non-Faradaic charge storage process [13]. Therefore, the alteration in the battery type component is the only way to increase the energy density for the desired level. Unfortunately, metal oxide or phosphate based insertion type materials are having either higher redox potential (>1 V *vs.* Li) or lower capacity (<400 mAh g^{-1}) or both [3,7,14,15]. Thus, working potential is diluted which eventually suppresses the net energy density of LIC. Even though, graphite or hard carbon based systems exhibits working potential close to metallic Li, but the power density is found inferior. Therefore, a paradigm shifts of traditional intercalation to alloying mechanism are desperately required the electrode composed of high capacity (>600 mAh g^{-1}) with lower working potential (<0.5 V *vs.* Li) is warranted to realize the goal.

In this line, sn-based derivatives like SnO_2 is found to appealing in terms of high capacity (782 mAh g^{-1} for $Li_{22}Sn_5$), lower working potential (~0.25 V *vs.* Li), naturally abundant, and eco-friendly [16–18]. However, huge irreversible capacity loss (ICL), volume expansion, pulverization and agglomeration of particles on cycling are the important issues for such alloying type anodes, but it can be effectively tackled by controlling the testing window, preparing nanostructured morphology with voids, and making composites with carbonaceous counterparts [19–22]. The Sn based nanostructures, particularly one dimensional structure are providing both large specific surface area and reduced Li-ion diffusion path which eventually translate better high current performances [23,24]. Further, modification like surface coating or doping can suppress the volume expansion, and/or maintain the stable microstructure for restraining during pulverization [25,26]. With respect to the cathodic side, the AC derived from various bio-sources are increasing interest as suitable cathode to be used as high energy LIC owing its lower cost, inherent heteroatom doping, naturally existing various functional groups, electrochemical stability and efficient recycling [27]. In this LIC, we have chosen, jackfruit skin derived AC as cathode along with the pre-lithiated SnO_2 as negative electrode [28]. Generally, just pre-lithiation is sufficient for graphite/hard carbon, while employing alloy type negative electrode requires few cycles (may be 2 or 3) with Li and it is necessary for the complete elimination of ICL, besides the lithiation.

On the other hand, fabrication of high power and high energy LIB is also under serious investigation to drive the HEV and EV [3]. In this line, taking the advantages like high capacity, lower working potential and high power capability of alloy type materials, we attempted to explore the fabrication high performance LIB using pre-treated SnO_2 as negative electrode. The LIB assembly composed of homemade high voltage spinel ($Li_{0.995}V_{0.005}Ni_{0.5}Mn_{1.5}O_4$, LVNMO) as cathode (theoretical capacity ~ 147 mAh g^{-1}) [29,30]. Though, the performance of sn-C composite based practical cells is reported with $LiFePO_4$, $LiNi_{0.5}Mn_{1.5}O_4$ cathodes etc. [31,32], but, still SnO_2 holds its originality and novelty in terms of appreciable theoretical capacity, reaction mechanism and performance towards the fabrication high power LIB. For instance, in SnO_2, there is no compulsory requirement for carbon coating/composite compared to pure Sn metal, the formation of amorphous Li_2O matrix is sufficient to sustain the volume change observed during first discharge [16,33–35]. This certainly provides the necessary improvement in the volumetric capacity over sn-C composites.

Accordingly, the SnO_2 anode was prepared *via* a simple precipitation route and calcined at different temperature conditions. Li-storage profiles of SnO_2 were examined in half-cell assembly with Li in presence of three different electrolyte solution and different loadings of conductive additive. Similarly, the counter electrodes like AC and LVNO were also tested with Li to adjust loading during the fabrication of LIC and LIB assembly, respectively. Either the negative electrode, SnO_2 was pre-treated or lithiated prior to the fabrication of said assemblies. Apart from this, a symmetric supercapacitor was also carried out using Jackfruit derived AC for the comparison of energy and power densities of LIB and LIC. Apparently, SnO_2 based LIC perfectly lies between the two-prominent high power (supercapacitor) and high energy (LIB) storage devices. Extensive structural, morphological and electrochemical studies were performed in both material and device point of view, and discussed in detail.

2. Materials and methods

2.1. Preparation of SnO_2 nanorods bundle (SOB)

Marine algae inspired SnO_2 nanorods bundle were synthesised *via* a slightly modified method developed by Han, et al., [36]. Firstly, 5.5 mmol oxalic acid and 0.5 mmol adipic acid were dissolved in 60 ml of mixed solution contains 5:1 vol ratio of ethanol and PEG400. Then, 7 mmol $SnCl_2{\cdot}2H_2O$ was added to the above solution with continuous stirring, and few minutes later, 15 ml of distilled water was added dropwise. The final mixture was transferred into a 500 ml Teflon lined autoclave and kept at 80 °C for 4 h. The resultant grey coloured precipitates were washed several times with ethanol and then dried at 60 °C for 10 h under vacuum. Finally, the products were calcined using box furnace at different temperatures 500, 550 and 600 °C for 3 h in air and designated as SOB-1, SOB-2 and SOB-3, respectively. Jack fruit peel derived AC (JF-AC) and high voltage spinel (LVNMO) preparations were described in our earlier reports [28–30].

2.2. Physical characterization

Crystalline phase of the resultant material was studied by powder X-ray diffraction (XRD, Rint 1000, Rigaku, Japan) using CuK_α radiation. BET surface area measurements were carried out using a Micromeritics ASAP 2010 surface area analyzer. Morphological features of the samples were recorded by using a field emission scanning electron microscope (FE-SEM, S4700, Hitachi, Japan) and transmission electron microscopy (TEM, TecnaiF20, Philips, Holland). X-ray photoelectron spectroscopy (XPS) was also

performed using a Multilab 2000, (Thermo Scientific, UK) with monochromator and Al kα radiation ($h\nu$ = 1486.6 eV).

2.3. Electrochemical characterization

Both positive and negative electrodes were formulated with active materials (60–72%), ketzen black (KB, 14–24%) as conductive additive, and teflonized acetylene black (14–16% of TAB-2) as binder with ethanol. The slurry was pressed over a stainless-steel mesh (16 mm diameter, 200 mm^2 area) and then dried at 160 °C for 4 h in vacuum oven [27,29]. All the electrochemical measurements performed in a standard CR 2032 coin-cell and the cells are assembled in Argon-filled glove box. For LIC and LIB assembly, the cathode mass (both JF-AC and LVNMO) loading were adjusted with respect to the counter electrode, SOB (after pre-lithiation the electrode mass calculation based on the alloying reaction). Both electrodes separated by a porous polypropylene (Celgard 3401, USA) film and filled with liquid electrolytes. Here, we used three kind of electrolytes solutions *i.e.* **E1** [1 M $LiPF_6$ in (1:1 v/v) ethylene carbonate (EC)/di-methyl carbonate (DMC)], **E2** [1.2 M $LiPF_6$ in (2:2:6 v/v/v) EC/ethyl methyl carbonate (EMC)/DMC + $LiBF_4$ (0.2) +PS (1.0)+TMSPi (0.5)+FEMP (0.3)+FEPA (0.1) and **E3** [1 M $LiPF_6$ in (1:2 v/v) EC/DMC] from Soulbrain Co. Ltd, South Korea. Cyclic voltammetry (CV) and electrochemical impedance spectroscopy (EIS) studies were performed using an electrochemical work station (Bio-Logic (SP-150), France). Galvanostatic charge-discharge studies were performed at different current densities using a conventional battery tester (WBCS 3000, Won-A-Tech, Korea) under ambient conditions.

3. Results and discussion

3.1. Physical studies

Structural characterization of as synthesised SOBs was analysed by XRD technique and shown in Figs. 1 and S1a. Fig. S1a shows the combined XRD patterns of SOBs treated at different calcination temperature. The XRD pattern clearly revealed the presence of mixed crystalline phases which are indexed according to tetragonal (ICDD 00-041-1445) and orthorhombic (00-029-1484) structures. The tetragonal geometry appears to be dominant for all the SOBs prepared. Fig. 1 shows the Rietveld refined XRD pattern of SOB-2. The mixed phases are identified via the refinement and estimated the composition of 87.17 and 12.83% for *$P4_2/mnm$* and *Pbcn* space groups, respectively. The orthorhombic (*Pbcn*) phase is a secondary phase which usually forms at high pressure and temperatures conditions. However, here, surprisingly, the low temperature condition and synthesis procedure also triggers the formation of such crystalline rutile phase. The lattice parameters and unit cell volume of the two phases are given in Table-S1. Besides the crystalline phase (single or mixed), SnO_2 structure will be collapsed (not morphology) during the alloy formation (Li_xSn), and prevented them to oxidize upon charge process by controlling the testing potential, since the Sn^0 will be oxidized beyond ~1 V *vs.* Li. Therefore, whatever may be the crystalline phase; it will be destroyed during first discharge. As a result, crystalline phase not played an important role towards the sustained Li-storage *via* alloying mechanism which we clearly observed for SnO_2 earlier [22,35,37,38].

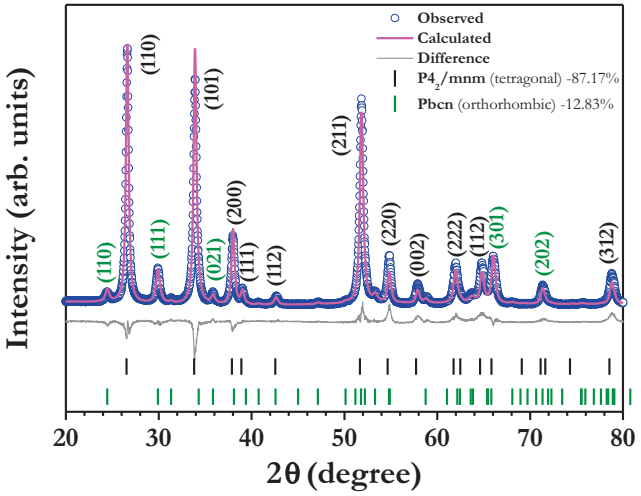

Fig. 1. The Rietveld analysis of SnO_2 nanorods bundle (SOB-2).

Surface morphology and microstructure of SOBs were investigated by FE-SEM and TEM with different magnifications. From Figs. 2a and S2, FE-SEM images clearly showed a complete structure of the SnO_2 nanorods bundle. Initially, the SnO_2 nanorods formed by a serially connected primary nanoparticles under controlled atmospheric conditions and a bundle shape were assembled by the self-orientation of such nanorods. The thermal energy (from 4 h incubation) is eventually leads to the marine algae-like bundle shaped morphology of SnO_2 [39]. When the sintering temperature is increased from 500 to 600 °C, more roughness of the surface and porous nature is clear. On careful examination of the TEM analysis (Fig. 2b), the SOB consists of numerous primary nanoparticles in the range of few nanometres are assembled together. The average length and diameter of the nanorods is found approximately 2–3.5 and 0.2–0.3 μm, respectively. Fig. 2c shows the HR-TEM image and the observed lattice fringes are 0.34 and 0.18 nm, which is consistent with the reflections of (1 1 0) and (2 2 0) crystal planes. The selected area electron diffraction pattern (SAED) pattern (Fig. 2d) reveals the presence of polycrystalline nature of SnO_2, and the corresponding reflections are well-matched with the tetragonal phase (ICDD 00-041-1445).

Chemical composition and oxidation state of elements of SOB-2 was analysed by XPS and shown in Fig. 3. Fig. 3a shows the survey spectrum of SOB-2 which composed of Sn, O and C elements, and no other impurities. The high resolution Sn 3d spectrum is shown in Fig. 3b, which can be fitted into two peaks in the region of ~486.59 and 495.06 eV and assigned to the binding energy of Sn $3d_{5/2}$ and Sn $3d_{3/2}$, respectively [40,41]. This clearly suggests that only the Sn^{4+} species exist in SOB-2. Fig. 3c shows the O 1s spectrum is de-convoluted into three peaks ~530.48, 531.68 and 533.03 eV and it can be attributed to M-O, C—O and H—O bonds, respectively. In addition, the C 1s is also de-convoluted into three more peaks centred at ~284.6, 286.35 and 288.64 eV which corresponds to —C=C— (sp^2), O—C (sp^3) and C=O, respectively. The amount of carbon in SOB-2 was estimated by TGA analysis and represented in Fig. S1b. A gradual weight loss about ~1.4 wt.% was observed between 25 and 700 °C and it is likely related to the removal of water and carbon traces from SOB-2.

The N_2 gas adsorption/desorption isotherm and pore size distribution of all SOBs is collected from the BET analysis at a given pressure and depicted in Fig. S2. For all SOBs samples (P/P_o ~ 0.8 to 0.99) exhibits a similar type IV isotherm indicating the presence of mesoporous structure. The BET specific surface area, total pore volume and average pore diameter of all SOBs are given in Table S2. Apparently, the BET surface area of the SOBs are found to be 15–18 $m^2\,g^{-1}$ *i.e.* decreasing the temperatures results an increasing the surface area.

3.2. Half-cell performance of SnO_2

Prior to the fabrication LIC and LIB, Li-storage properties of the SOBs must be assessed for the mass balance which is essential to

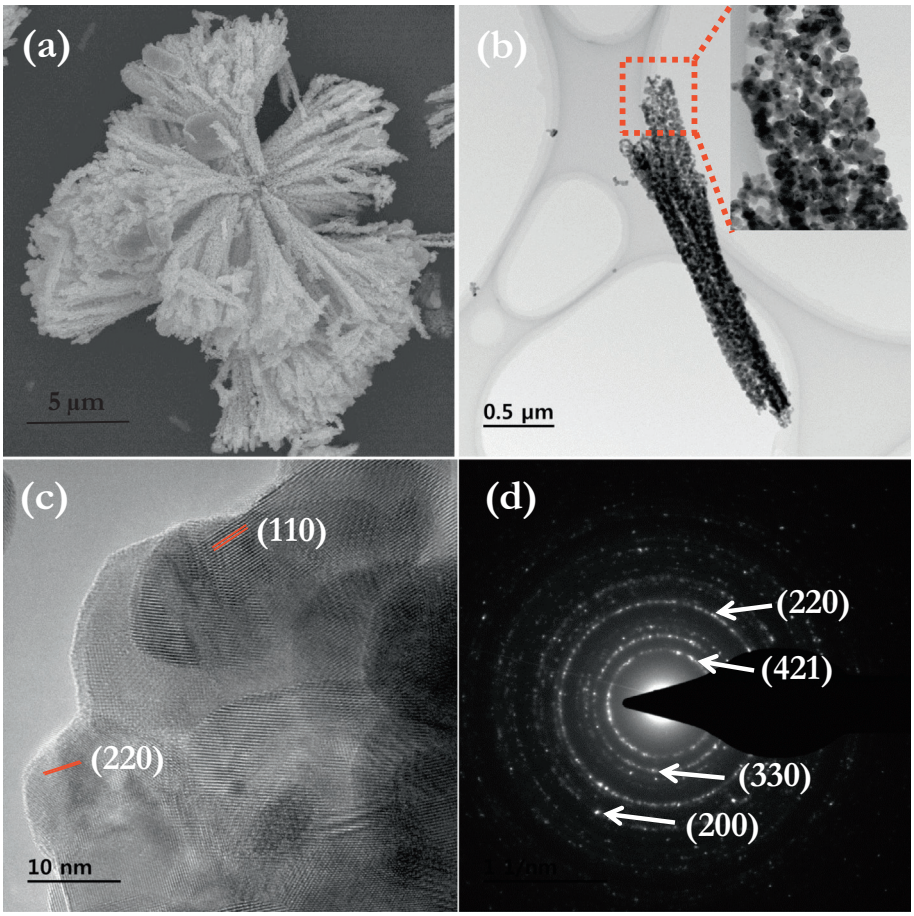

Fig. 2. (a) FE-SEM images, (b & c) low and high magnification TEM image, and (d) SAED pattern of SOB-2.

realize the higher energy density values. Therefore, Li-storage properties of as synthesised SOBs were evaluated in half-cell configuration *vs.* Li within the restricted potential window of 5–800 mV (Figs. 4 and S4). Figs. 4a and S4 represents the galvanostatic cycling and charge/discharge profile of SOB-1, SOB-2 and SOB-3 with 14 wt.% of KB in E2 electrolyte at current density of 0.1 A g^{-1}. The 1st, 2nd and 70th cycle discharge capacity of SOB-2 was found 2697, 695 and 628 mAh g^{-1}, respectively. The capacity retention at 70th cycle for SOB-2 is ~90%, whereas 84 and 82% of capacity is retained for SOB-1 and SOB-3 (capacity retention calculated from the 2nd cycle), respectively. There is no obvious difference between the capacity profiles is noted in initial cycles, but SOB-2 rendered better cycleability than other two. This is mainly due to the structural integrity with optimum crystallinity, surface area and active sites for the electrochemical reaction compared to other two conditions. Therefore, the influence of conductive additive (KB) on the electrochemical performance of SnO_2 has been conducted only for SOB-2. The KB concentration has been increased from 14 to 24 and 33 wt.% during the formulation of the electrode and studied with the same E2 solution. Compared to 14 and 33 wt.% loading, the 24 wt.% KB exhibits better electrochemical characteristics, for example, the discharge capacity of 628 mAh g^{-1} is noted in the 70 cycles with ~2.5% higher capacity than the 14 wt.% loaded SOB-2.

By keeping the same loading *i.e.* 24 wt.% KB, the SOB-2 electrodes were subjected for further studies with various electrolyte solutions (E1, E2 and E3) and corresponding cycle behaviours are shown in Fig. 4c. Clearly, the SOB-2 tested with E2 electrolyte delivers a capacity of 628 mAh g^{-1} after 70 cycles with stable cycling profile at a current density of 0.1 A g^{-1}. In contrast, the irregular capacity profile with ~17 and 12.6% lower capacity was observed while testing in E1 and E3 based solutions, respectively. Figs. 4d and S5a, shows a typical galvanostatic charge/discharge profile of SOB-2 with 24 and 14 wt.% KB electrodes in E2 electrolyte, respectively. The higher Li-storage with improved coulombic efficiency could largely attributed to the SnO_2 nanorods composed bundle and the choice of using the high voltage E2 electrolyte with restricted potential range [35]. Nevertheless, the 1D nanorods can able to provide the direct pathway for charge transport with shortened Li-ion diffusion pathways [42,43].

To elucidate the Li-storage mechanism in SOB-2, the CV studies were conducted between 5 and 800 mV *vs.* Li at a scan rate of 0.1 mV s^{-1} and depicted in Fig. S5b. The first cathodic sweep consists of two broad peaks centred at ~0.78 and 0.18 V *vs.* Li with larger current (area underneath the curve) response. This process is associated with the reduction/decomposition of the electrolyte and subsequent solid electrolyte interface formation. At the same time, structural destruction of the SnO_2 is also takes place along with alloy formation (Li_xSn) with Li at 0.2 V *vs.* Li and amorphous Li_2O matrix as well. This reaction can be described schematically as $SnO_2 + 8.4\ Li^+ + 8.4\ e^- \rightarrow Li_{4.4}Sn + 2Li_2O$. The whole activity eventually leads to the consumption of large number of Li-ions in irreversible manner. Thus, huge irreversible capacity loss is noted which is clear from the galvanostatic cycling irrespective of the synthetic protocols. However, in the subsequent cycles, CV curve clearly shows only a pair of peaks positioned at ~0.14 and 0.55 V *vs.* Li during cathodic and anodic sweep, which corresponds to the reversible alloying and de-alloying reaction ($Li_{4.4}$-

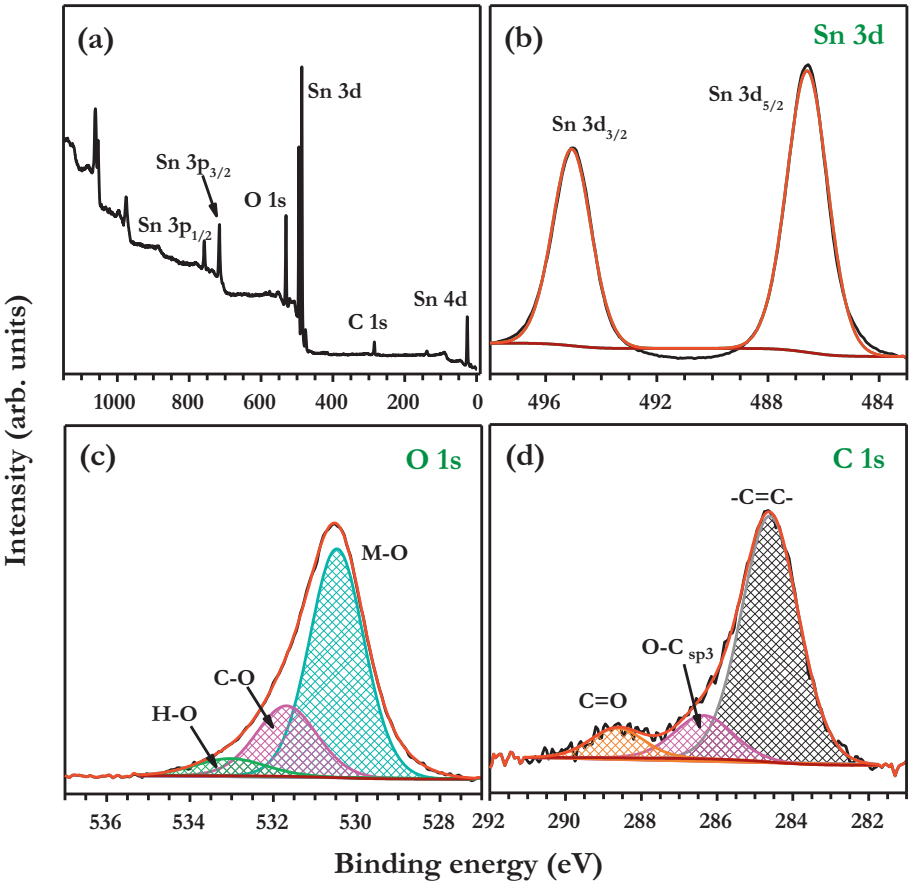

Fig. 3. XPS analysis of SOB-2 (a) survey spectrum consist different elements (b) Sn 3d, (c) O 1s, and (d) C 1s.

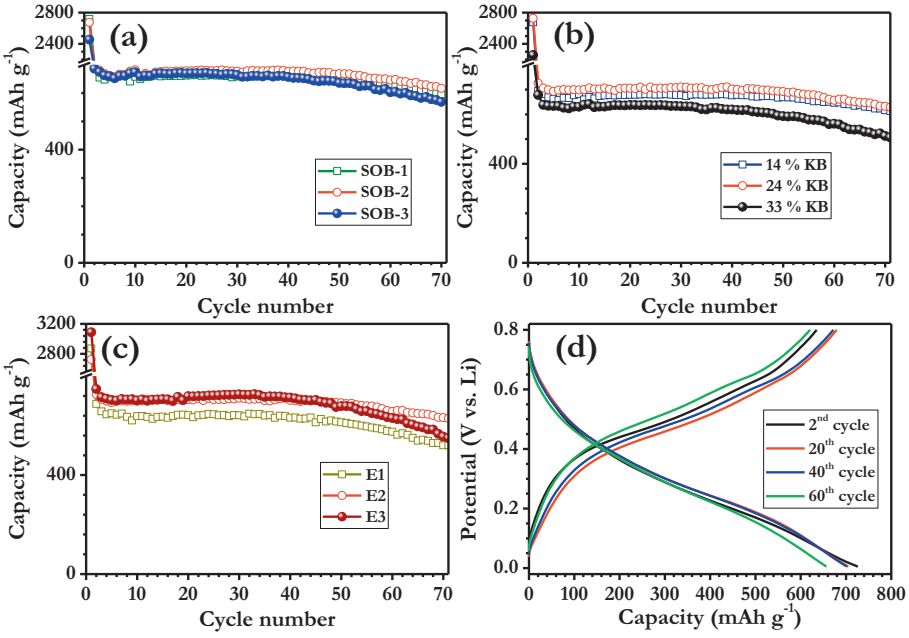

Fig. 4. (a) Cycling performance of SOB prepared at different temperatures with 14 wt.% of KB in E2 electrolyte at current density of 0.1 A g^{-1}, (b) Electrochemical performance of SOB-2 with different weight percentage of KB (14, 24 and 33 wt.%) in E2 electrolyte at current density of 0.1 A g^{-1}, (c) Performance of SOB-2 in different electrolytes E1, E2 and E3 with 24 wt.% KB at current density of 0.1 A g^{-1}, and (d) Typical charge-discharge curve of SOB-2 with 24 wt.% of KB in E2 electrolyte between 5 and 800 mV at current density of 0.1 A g^{-1}.

$Sn \leftrightarrow Sn^0 + 4.4\ Li^+ + 4.4\ e^-$) [44]. The observed peaks position in the 10th cycle is very close to the 2nd cycle, reflecting a good reproducibility and stable performance of SOB in Li_2O matrix. The Nyquist plots of SOB-2 with 24 wt.% of KB electrodes in E2 electrolyte before and after 10 cycles are as shown in Fig. S5c. The spectrum consists of a depressed semicircle in the medium-to-high frequency region and an inclined vertical tail in the low frequency range. The fresh and cycled cell exhibits both solution (R_s) and charge transfer resistance (R_{CT}) of 6.22 (9.04) and 33.71 (20.91) Ω, respectively. From this, we inferred that cycled electrode exhibit smaller semicircle *i.e.* lower R_{CT} than fresh cell, suggesting a better ionic and electronic conductivities at the interface and grain boundaries of SnO_2 nanoparticles. This is mainly because of the stabilized SEI layer formation over the electro-active material surface after few initial cycles.

3.3. Li-ion capacitor (LIC)

Electrochemical energy storage devices exhibiting higher energy density with lower power capability is not sufficient to drive high end applications like EV and HEV, but can able to power miniature devices. Poor rate capability is one of the prime issues for both LIC and LIB which composed of graphite as negative electrode. Thus, introduction of high capacity, conversion or alloying type materials are anticipated to provide the required enhancement in power capability without compromising the energy density. In this line, we tried to exploit the possibility of using such high capacity alloy type SnO_2 as battery type negative component in LIC configuration. On the other hand, biomass derived, JF-AC is utilized as supercapacitor component which was prepared according to our previous report [28]. Though, the synthesis procedure and supercapacitor studies were reported, but the studies are limited to aqueous medium only. Prior to this LIC assembly, the mass loading of positive (q_+) and negative (q-) electrodes should be balanced from the charges of each electrode to realize the higher energy density. Accordingly, the single electrode performance of JF-AC has been assessed with metallic Li between 2 and 4.5 V at current density 0.1 A g^{-1} in E2 electrolyte (Fig. S6). Apparently, JF-AC delivered good cycling performance and high reversibility (~98 mAh g^{-1}). The linear variation of charge-discharge curves clearly represents the double layer formation across the electrode/-electrolyte interface with specific capacitance of ~141 F g^{-1}. Based on the single electrode (half-cell) performance of both electrodes, the mass loading between anode and cathode has been adjusted to 1:7 ratios (2.5:17.5 mg). Prior to the assembly, SnO_2 anode has been pre-lithiated by conducting half-cell assembly with Li. In typical process, two complete galvanostatic cycle has been conducted at 0.1 A g^{-1}, and carefully dismantled in discharged state (5 mV *vs.* Li) to pair with JF-AC.

Figs. 5a and S7a shows the CV studies of LIC recorded at different scan rates (1, 2, 5, 10 and 20 mV s^{-1}) between 1.7 and 4.2 V. The CV curves of LIC clearly depicts the combined charge storage mechanism *i.e.* both (de-)alloying and double layer behaviour. Appearance of distorted CV profiles signifies the involvement of two different charge storage mechanism in LIC, for example, adsorption of PF_6^- in cathode and de-alloying ($Li_xSn \rightarrow Sn^0 + x\ Li^+ + x\ e^-$) reaction on counter electrode. Alloying ($Sn^0 + x\ Li^+ + x\ e^- \rightarrow Li_xSn$) and PF_6^- desorption is noted during discharge process. When the sweep rates increased, the shapes of CV curves are broadened and the shifting of peak position towards lower potential is noted. This deviation is expected, due to the increase in electrode polarization upon high current testing. Galvanostatic studies for LIC is performed at different current rates between 1.7 and 4.2 V and illustrated in Fig. 5b and S8b. The applied current densities are based on the total mass loading of both electrodes. Irrespective of current rates, charge/discharge curves showed a two

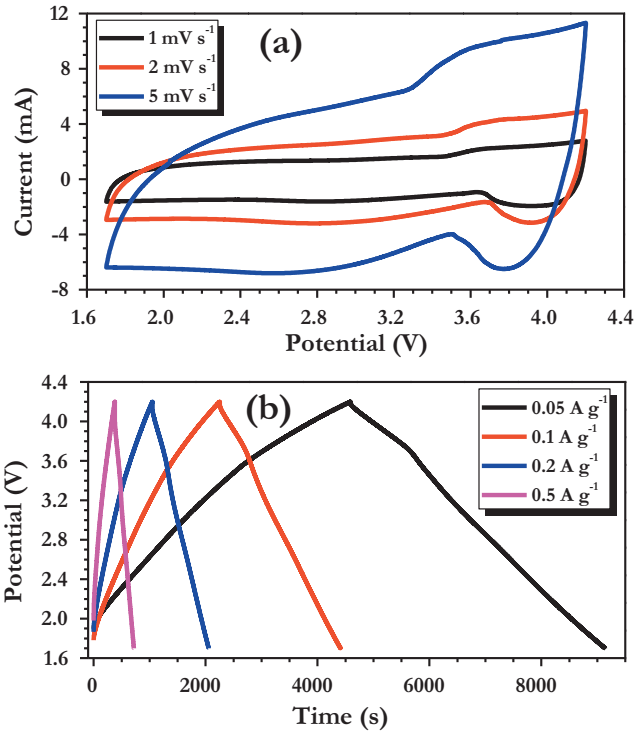

Fig. 5. (a) Cyclic voltammetry traces of pre-lithiated SnO_2 and JF-AC based LIC at different scan rates in E2 electrolyte, and (b) Typical galvanostatic charge-discharge curves of LIC at various current rates.

voltage stages in the range of 4.2 to 3.7 and 3.7 to 1.7 V, which is consistent with CV traces. Fig. 5b and S7b shows the increase of applied currents from 0.05 to 1.25 A g^{-1}, the internal resistance of the electrode has been raised and/or confirmed from the IR drops in the discharge curves. From the charge-discharge curves, the energy and power densities of LIC were calculated based on the following equations,

$$\text{Power density} = \frac{i(A) \times \Delta V}{m(mg) \times 10^{-6}} (\text{W kg}^{-1}) \quad (1)$$

$$\text{Energy density} = \frac{Power\ density \times \Delta t}{3600} (\text{Wh kg}^{-1}) \quad (2)$$

where, **I** is applied current (A), **t** is discharge time (s), **m** is total weight of active materials in both electrodes, **ΔV** is average working potential. Pre-lithiated SnO_2/JF-AC based LIC is callable of delivering the maximum energy density of 187 Wh kg^{-1} at low currents, even at high power density 3.7 kW kg^{-1}, the energy density will remain at 90 Wh kg^{-1}. The observed values are high and significant compared to the insertion type electrode explored for LIC point of view [7,10]. Detailed discussions are given in the forthcoming section.

Like high energy and power capability, durability is equally important for the electrochemical energy storage devices. Hence, galvanostatic charge/discharge measurements were conducted at current density of 0.5 A g^{-1} to evaluate the cycle durability, and columbic efficiency and given Fig. 6a. The LIC displayed an excellent cycling profile and rendered ~80% of its original value after 10,000 cycles with columbic efficiency over 99%. This is one of the excellent cycleability reported for LIC irrespective of the battery type electrodes employed and its storage mechanism [7,10]. The Nyquist plots are also recorded for LIC before and after 10,000 cycles to correlate the obtained results and presented in Fig. 6b. It shows a semicircle in the high-frequency region and an inclined straight line in the low-frequency region. The R_{CT} value

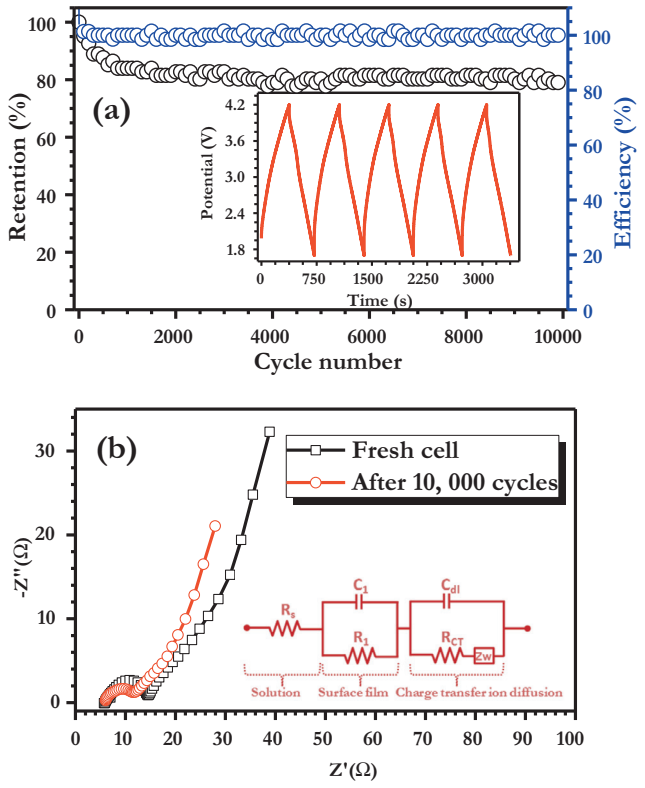

Fig. 6. (a) Cycling profiles of pre-lithiated SnO_2 and JF-AC based LIC at current density of 0.5 A g^{-1} in E2 electrolyte, and (b) Nyquist plot of LIC recorded before and after 10,000 cycles with corresponding equivalent circuit.

of LIC cell after cycling has been decreased from 14.58 to 11.75 Ω which is consistent with the half-cell performance of SnO_2. Though the supercapacitor component, JF-AC is involved in the electrochemical reaction, but purely in physi-sorption process. Hence, much variation in impedance properties are originated from the alloy type SnO_2 only. As mentioned earlier, the stabilized SEI formation over alloy type anode, certainly promotes the reduction in R_{CT} values which eventually facilitates the charge transfer process upon cycling.

3.4. Li-ion battery (LIB)

One of the prominent, extensively studied high voltage (4.7 V *vs.* Li) and high rate cathode is spinel $LiNi_{0.5}Mn_{1.5}O_4$ which exhibits higher redox potential, than the conventional carbonate based electrolyte solution [45]. Moreover, it also suffers Mn dissolution and poor elevated temperature issues. In this line, we made an attempt to improve the said properties by V doping in Li sites, which eventually translates better electrochemical profiles at both ambient and elevated temperature conditions and minimizes the Mn dissolution as well [29]. Though LVNMO cathode is capable of delivering the maximum energy density of ~696 Wh kg^{-1}, but finding the suitable anode to realize above energy density is a hot topic of research today [46–48]. Amongst, alloy type sn-C and Si, insertion type TiO_2-B and $Li_4Ti_5O_{12}$ anodes are worth mentioning. Nevertheless, the usage of insertion type anodes with $LiNi_{0.5}Mn_{1.5}O_4$ are studied extensively, but the energy density is drastically diluted due to the higher redox potential of the $Ti^{4+/3+}$ couple [3,48]. Therefore, utilization of alloying type anodes with $LiNi_{0.5}Mn_{1.5}O_4$ cathodes is highly promising. Unfortunately, both metallic Sn and Si requires a strong carbon environment to overcome the volume variation and consequently to display a better electrochemical stability [17,49]. By considering the advantages of Sn, we attempted to utilize the SnO_2 as negative electrode, which eventually forms an amorphous Li_2O phase during first discharge. We certainly feel that the presence of Li_2O matrix and restricted potential is sufficient to provide good electrochemical activity which is clearly evident from LIC performance and in our previous work as well [35]. Like LIC, the mass loading between anode to cathode (Fig. S8) was adjusted based on the electrochemical performance with respect to the metallic Li and fixed in the ratio of 1:5 is (anode is 2.5: cathode is 12.5 mg). Prior to the fabrication, the SnO_2 is pre-treated with Li to eliminate the ICL by conducting the two-complete charge-discharge cycles and coupled with LVNMO in the presence of E2 electrolyte and given in Fig. 7. Fig. 7a shows the CV curves of LVNMO/pre-treated SnO_2 based LIB cell recorded between 3.7 and 4.7 V at scan rate of 0.1 mV s^{-1}. The CV traces displayed a pair of peaks located at 4.58 and 4.15 V corresponds to the alloying and de-alloying process. Simultaneously, the $Ni^{2+/4+}$ redox couple is also occurred on the cathodic side and it is reversed during discharge process. However, there is no remarkable change in the area underneath the curve upon cycling indicates the excellent stability of both cathode and anode. In contrast to LIC, the increase in R_{CT} values are observed for LIB after 10 cycles, for example from the Nyquist plots 14.9 and 18.3 Ω are registered before and after 10 cycles (Fig. 7b). Since, both SnO_2 and LVNMO obey the Faradaic reaction. Upon pre-treatment of SnO_2 electrodes, the SEI layer is formed, and it has been eventually paired with freshly made LVNMO cathode. According to the half-cell performance (cell chemistry), SEI layer will also form in the cathodic side as well irrespective of the capacity is decreased or increased. Thus, increase in R_{CT} values are noted for LVNMO/pre-treated SnO_2 based LIB cell. In the case of LIC, SnO_2 only involved the Faradaic reaction, whereas JF-AC contributes the non-Faradaic charge storage *i.e.* physi-sorption. In addition, $Ni^{2+/4+}$ redox couple occurs beyond the thermodynamic stability window of the solution, which eventually leads to the decomposition of electrolyte and subsequent formation of SEI layer over cathodic particles. Thus, the increase in R_{CT} trend was noted. Fig. 7c shows the charge-discharge curves of LIB measured between 3.7 and 4.7 V at current density of 0.1 mA g^{-1} (based on the cathode weight). The LVNMO/pre-treated SnO_2 based LIB cell delivered the discharge capacity of 86, 94 and 94 mAh g^{-1} for 2nd, 20th and 40th cycle, respectively. As expected, very high Coloumbic efficiency is noted upon cycle, for example first cycle it reaches ~82%, and substantially improved to >98% in the following cycles. The less efficiency in the first cycle is mainly due to the re-filling of the fresh electrolyte solution and higher redox potential of $Ni^{2+/4+}$ couple cannot be ruled out. Apparently, the monotonous charge-discharge curves are noted and consistent with the broad oxidation and reduction peaks observed during CV analysis. For easier comparison, the capacity values are also calculated based on the total mass (anode + cathode), cathode, and anode. The cycling performance and columbic efficiency of LIB is displayed in Fig. 7d. It is worth noting that the capacity trend showed a gradual increase in capacity profile for initial cycles and thereafter starts declining which is like those of half-cell performance of LVNMO. As expected, a gradual decrease in cycling profiles is noted owing to the higher redox potential of $Ni^{2+/4+}$couple than the decomposition potential of the electrolyte.

Rate capability studies of LIB is also performed between 3.7 and 4.7 V at different current rates (based on the total weight of electrodes) and depicted in Fig. 8. It is obvious to note that the increase in current density tends to decrease in capacity profile with increase in polarization. For instance, the discharge capacity of 94 mAh g^{-1} is noted at a current density of 16 mA g^{-1}, and then decreased to 85, 71, 55, 27 and 8 mAh g^{-1} at current densities of 32, 81, 161, 323 and 645 mA g^{-1}, respectively. The high working

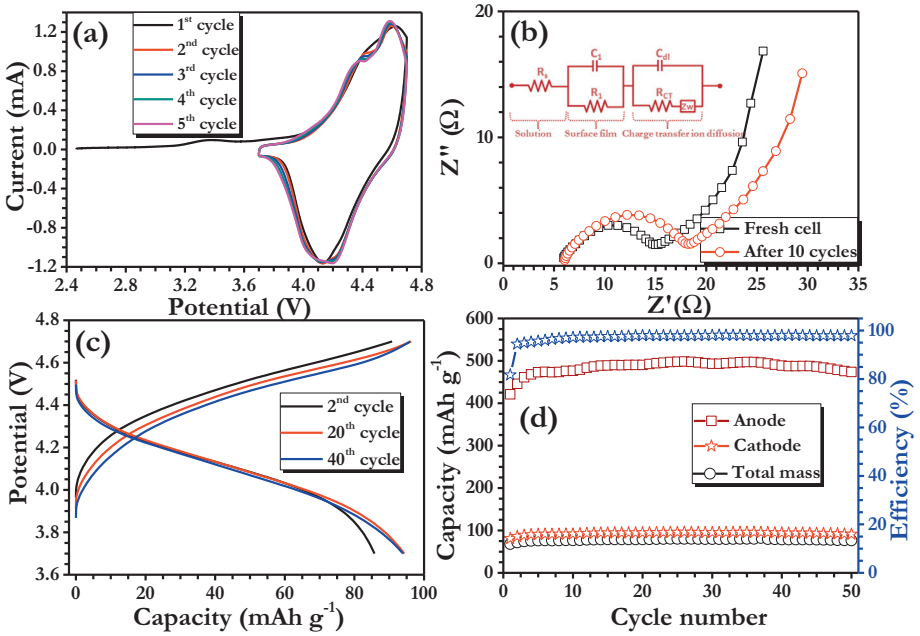

Fig. 7. (a) Cyclic voltammetry traces of pre-treated SnO_2 and $Li_{0.95}V_{0.05}Ni_{0.5}Mn_{1.5}O_4$ based LIB recorded at scan rate of 0.1 mV s^{-1} in E2 solution, (b) Nyquist plots measured before and after 10 cycles with equivalent circuit, (c) Typical charge-discharge recorded at current density of 0.1 A g^{-1}, and (d) Cycleability of pre-treated SnO_2 and $Li_{0.95}V_{0.05}Ni_{0.5}Mn_{1.5}O_4$ based LIB between 3.7 and 4.7 V.

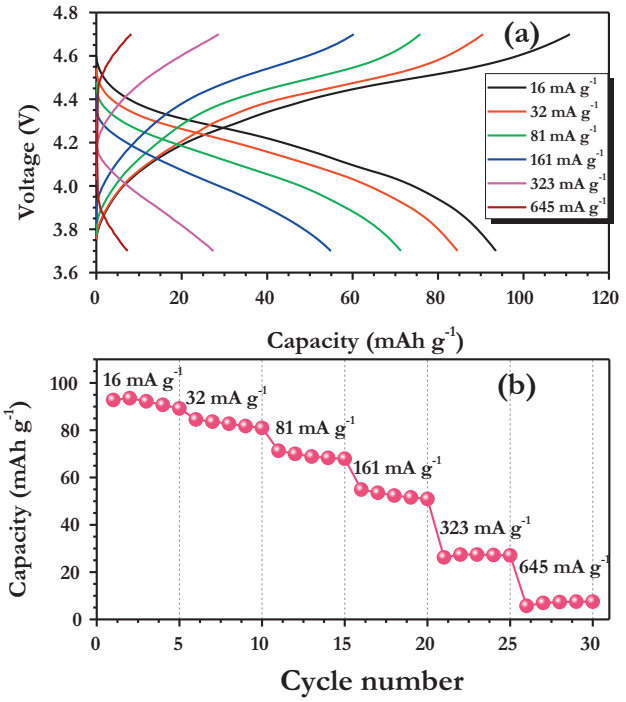

Fig. 8. (a) Typical **c**harge-discharge curves of pre-treated SnO_2 and $Li_{0.995}V_{0.005}Ni_{0.5}Mn_{1.5}O_4$ based LIB recorded at various current densities (based on total mass is 15 mg), and (b) plot of discharge capacity *vs.* Cycle number for pre-treated SnO_2 and $Li_{0.95}V_{0.05}Ni_{0.5}Mn_{1.5}O_4$ based LIB between 3.7 and 4.7 V.

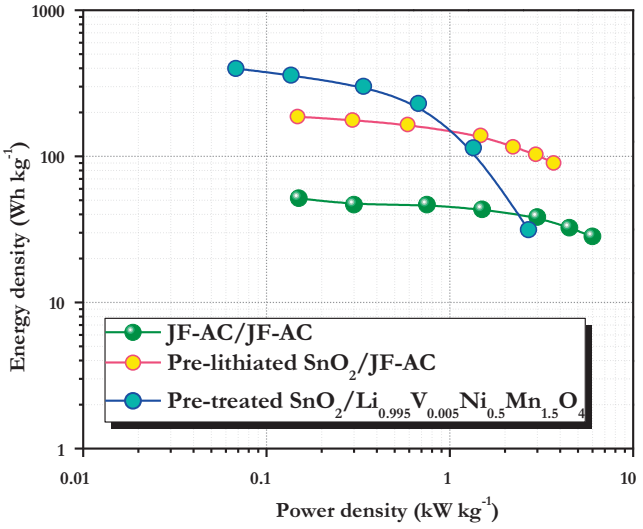

Fig. 9. Ragone plot shows the comparison of energy and power densities of supercapacitor (JF-AC/JF-AC), Li-ion capacitor (Pre-lithiated SnO_2/JF-AC), and Li-ion battery (Pre-treated SnO_2/$Li_{0.995}V_{0.005}Ni_{0.5}Mn_{1.5}O_4$) with E2 solution.

voltage (4.27 V) and specific capacity values are reflecting with an energy density as high as 399.5 Wh kg^{-1}.

Ragone plots of LIC and LIB are compared and shown in Fig. 9. Further, the performance of JF-AC based symmetric supercapacitor (SC) is also studied with same E2 electrolyte and compared (Fig. S9). The energy density can approach 187, 399.5 and 51.5 Wh kg^{-1} for LIC, LIB and SC, respectively. Certainly, the observed energy density is one of the best values reported for LIC assembly irrespective of the battery type components used, to date [5,7,10]. Even at high power (3.7 kW kg^{-1}), the energy density remains at ~90 Wh kg^{-1} for LIC which is quite remarkable. The significantly improved electrochemical performance of energy device, especially LIC is mainly attributed to the mesoporous structure of SnO_2 nanorods bundle with a variety of favourable properties are ascribed here. Firstly, we controlled the alloying/de-alloying reaction of SnO_2 with restricted potential by preventing them to oxidize into native oxides like SnO and SnO_2. Secondly, the mesoporous rod like structure allows complete access of the active materials by the electrolyte charge carriers and acting as buffer

matrix to sustain the volume variation. In addition, the presence of amorphous Li_2O matrix is also extends its support during volume variations. Also, the high surface area carbons derived from bio-waste can also accumulate more number of charge carriers on the surface, which cannot be ruled out. Finally, the electrolyte solution composed of different additive and compositions is also one of the reasons to improve the performance and cycling stability of the practical energy devices irrespective of the configurations like LIC, LIB and SC.

4. Conclusion

We have designed the marine algae inspired SnO_2 nanorods bundle as an effective anode for practical high energy electrochemical storage devices. Influence of synthesis temperature, conductive additive and electrolyte on the performance of alloying/de-alloying reaction of SnO_2 was examined as negative-electrode. Presence of porous structure and discharge product (Li_2O) can able to accommodate the volume variation during alloying/de-alloying reaction. The optimized SOB-2 anode was coupled with jack fruit derived activated carbon and LVNMO cathodes towards the fabrication of LIC and LIB, respectively. Pre-lithiated SnO_2 coupled with JF-AC delivered an excellent long term cycling stability with retention of 80% initial values after 10,000 cycles. Even at high power (3.7 kW kg^{-1}), very high energy density is retained (90 Wh kg^{-1}) for LIC. Also, pre-treated SnO_2 with LVNMO in LIB assembly presents a high-energy density of 400 Wh kg^{-1}. This study clearly brings forth the information that alloy type negative electrode could be efficiently used to fabricate the high energy electrochemical storage devices with high power capability as well. Further, this also provides the exploration of high energy and high power LIC and LIB assemblies by using various kinds alloy type materials and intermetallic compounds.

Acknowledgements

This work was supported by the National Research Foundation of Korea (NRF) grant funded by the Korean Government (Ministry of Science, ICT and Future Planning) (No. 2016R1A4A1012224).

Appendix A. Supplementary data

Supplementary data associated with this article can be found, in the online version, at http://dx.doi.org/10.1016/j.cej.2017.05.003.

Reference

[1] J. Goodenough, J. Solid State Electrochem. 16 (6) (2012) 2019–2029.
[2] J.B. Goodenough, K.-S. Park, J. Am. Chem. Soc. 135 (4) (2013) 1167–1176.
[3] V. Aravindan, Y.-S. Lee, S. Madhavi, Adv. Energy Mater. 5 (13) (2015) 1402225.
[4] H. Jiang, H. Zhang, Y. Fu, S. Guo, Y. Hu, L. Zhang, Y. Liu, H. Liu, C. Li, ACS Nano 10 (1) (2016) 1648–1654.
[5] V. Aravindan, M. Ulaganathan, S. Madhavi, J. Mater. Chem. A 4 (20) (2016) 7538–7548.
[6] I. Plitz, A. DuPasquier, F. Badway, J. Gural, N. Pereira, A. Gmitter, G.G. Amatucci, Appl. Phys. A Mater. Sci. Process. 82 (4) (2006) 615–626.
[7] V. Aravindan, J. Gnanaraj, Y.-S. Lee, S. Madhavi, Chem. Rev. 114 (23) (2014) 11619–11635.
[8] G.G. Amatucci, F. Badway, A. Du Pasquier, T. Zheng, J. Electrochem. Soc. 148 (8) (2001) A930–A939.
[9] G.L. Soloveichik, Annu. Rev. Chem. Biomol. Eng. 2 (1) (2011) 503–527.
[10] K. Naoi, S. Ishimoto, J.-I. Miyamoto, W. Naoi, Energy Environ. Sci. 5 (11) (2012) 9363–9373.
[11] V. Etacheri, R. Marom, R. Elazari, G. Salitra, D. Aurbach, Energy Environ. Sci. 4 (9) (2011) 3243–3262.
[12] E.J. Cairns, P. Albertus, Annu. Rev. Chem. Biomol. Eng. 1 (1) (2010) 299–320.
[13] Y. Dai, L. Chen, V. Babayan, Q. Cheng, P. Saha, H. Jiang, C. Li, J. Mater. Chem. A 3 (42) (2015) 21337–21342.
[14] C. Masquelier, L. Croguennec, Chem. Rev. 113 (8) (2013) 6552–6591.
[15] S. Patoux, C. Masquelier, Chem. Mater. 14 (12) (2002) 5057–5068.
[16] A.D.W. Todd, P.P. Ferguson, M.D. Fleischauer, J.R. Dahn, Int. J. Energy Res. 34 (6) (2010) 535–555.
[17] M.N. Obrovac, V.L. Chevrier, Chem. Rev. 114 (23) (2014) 11444–11502.
[18] W.-J. Zhang, J. Power Sources 196 (1) (2011) 13–24.
[19] C.-M. Park, J.-H. Kim, H. Kim, H.-J. Sohn, Chem. Soc. Rev. 39 (8) (2010) 3115–3141.
[20] S. Goriparti, E. Miele, F. De Angelis, E. Di Fabrizio, R. Proietti Zaccaria, C. Capiglia, J. Power Sources 257 (2014) 421–443.
[21] M.N. Obrovac, L. Christensen, D.B. Le, J.R. Dahn, J. Electrochem. Soc. 154 (9) (2007) A849–A855.
[22] R. Hu, D. Chen, G. Waller, Y. Ouyang, Y. Chen, B. Zhao, B. Rainwater, C. Yang, M. Zhu, M. Liu, Energy Environ. Sci. 9 (2) (2016) 595–603.
[23] N.-S. Choi, Y. Yao, Y. Cui, J. Cho, J. Mater. Chem. 21 (27) (2011) 9825–9840.
[24] D. Zhou, W.-L. Song, L.-Z. Fan, ACS Appl. Mater. Interfaces 7 (38) (2015) 21472–21478.
[25] D. Zhou, W.-L. Song, X. Li, L.-Z. Fan, ACS Appl. Mater. Interfaces 8 (21) (2016) 13410–13417.
[26] D. Zhou, X. Li, L.-Z. Fan, Y. Deng, Electrochim. Acta 230 (2017) 212–221.
[27] P. Sennu, H.-J. Choi, S.-G. Baek, V. Aravindan, Y.-S. Lee, Carbon 98 (2016) 58–66.
[28] P. Sennu, V. Aravindan, Y.-S. Lee, J. Power Sources 306 (2016) 248–257.
[29] M.C. Kim, K.-W. Nam, E. Hu, X.-Q. Yang, H. Kim, K. Kang, V. Aravindan, W.-S. Kim, Y.-S. Lee, ChemSusChem 7 (3) (2014) 829–834.
[30] G.H. Lee, H.S. Kim, S.G. Baek, H.J. Choi, K.Y. Chung, B.W. Cho, S.Y. Lee, Y.-S. Lee, J. Power Sources 298 (2015) 379–384.
[31] S. Brutti, J. Hassoun, B. Scrosati, C.-Y. Lin, H. Wu, H.-W. Hsieh, J. Power Sources 217 (2012) 72–76.
[32] G.A. Elia, F. Nobili, R. Tossici, R. Marassi, A. Savoini, S. Panero, J. Hassoun, J. Power Sources 275 (2015) 227–233.
[33] I.A. Courtney, J.R. Dahn, J. Electrochem. Soc. 144 (6) (1997) 2045–2052.
[34] I.A. Courtney, J.R. Dahn, J. Electrochem. Soc. 144 (9) (1997) 2943–2948.
[35] V. Aravindan, K.B. Jinesh, R.R. Prabhakar, V.S. Kale, S. Madhavi, Nano Energy 2 (5) (2013) 720–725.
[36] Y. Han, X. Wu, Y. Ma, L. Gong, F. Qu, H. Fan, CrystEngComm 13 (10) (2011) 3506–3510.
[37] V. Aravindan, J. Sundaramurthy, E.N. Kumar, P.S. Kumar, W.C. Ling, R. von Hagen, S. Mathur, S. Ramakrishna, S. Madhavi, Electrochim. Acta 121 (2014) 109–115.
[38] A. Chaturvedi, V. Aravindan, P. Hu, R.R. Prabhakar, L.H. Wong, C. Kloc, S. Madhavi, Appl. Mater. Today 5 (2016) 68–72.
[39] L.X. Song, Z.K. Yang, Y. Teng, J. Xia, P. Du, J. Mater. Chem. A 1 (31) (2013) 8731–8736.
[40] M.J.K. Reddy, S.H. Ryu, A.M. Shanmugharaj, Nanoscale 8 (1) (2016) 471–482.
[41] W. Xia, H. Wang, X. Zeng, J. Han, J. Zhu, M. Zhou, S. Wu, CrystEngComm 16 (30) (2014) 6841–6847.
[42] D. Andre, S.-J. Kim, P. Lamp, S.F. Lux, F. Maglia, O. Paschos, B. Stiaszny, J. Mater. Chem. A 3 (13) (2015) 6709–6732.
[43] V. Aravindan, J. Sundaramurthy, P. Suresh Kumar, Y.-S. Lee, S. Ramakrishna, S. Madhavi, Chem. Commun. 51 (12) (2015) 2225–2234.
[44] S.Y. Hong, Y. Kim, Y. Park, A. Choi, N.-S. Choi, K.T. Lee, Energy Environ. Sci. 6 (7) (2013) 2067–2081.
[45] A. Manthiram, K. Chemelewski, E.-S. Lee, Energy Environ. Sci. 7 (4) (2014) 1339–1350.
[46] E.M. Erickson, C. Ghanty, D. Aurbach, J. Phys. Chem. Lett. 5 (19) (2014) 3313–3324.
[47] M.C. Kim, S.H. Kim, V. Aravindan, W.S. Kim, S.Y. Lee, Y.S. Lee, J. Electrochem. Soc. 160 (8) (2013) A1003–A1008.
[48] N. Arun, V. Aravindan, S. Jayaraman, N. Shubha, W.C. Ling, S. Ramakrishna, S. Madhavi, Nanoscale 6 (15) (2014) 8926–8934.
[49] F. Luo, B. Liu, J. Zheng, G. Chu, K. Zhong, H. Li, X. Huang, L. Chen, J. Electrochem. Soc. 162 (14) (2015) A2509–A2528.